Title: Whole brain wiring diagram of oxytocin system in adult mice

Abbreviated title: Brain wiring diagram of oxytocin system in mice

Seoyoung Son[1,*], Steffy B. Manjila[1,*], Kyra T. Newmaster[1], Yuan-ting Wu[1], Daniel J. Vanselow[2], Matt Ciarletta[1], Todd E. Anthony[3], Keith C. Cheng[2], and Yongsoo Kim[1]

1 Department of Neural and Behavioral Sciences, The Pennsylvania State University, Hershey, PA, USA, 17033

2 Department of Pathology, The Pennsylvania State University, Hershey, PA, USA, 17033

3 Program in Neuroscience, Harvard University, Boston, MA, USA, 02138

*Co-First author

Corresponding author:

Yongsoo Kim

Email: yuk17@psu.edu

Number of pages: 29

Number of figures: 5, tables: 2, and multimedia: 4

Number of words for abstract: 249, introduction: 501, and discussion: 1111

Conflict of interest statement: The authors declare no competing financial interests.

Acknowledgments

This publication was made possible by an NIH grant R01MH116176 to Y.K. and an NIH grant R24OD18559 to K.C. Its contents are solely the responsibility of the authors and do not necessarily represent the views of the funding agency. We thank Dr. Gloria Choi for kindly sharing OT-Cre transgenic mice and Rebecca Betty for assistance in editing the manuscript. We acknowledge use of computational resources in the High Performance Computing cluster at the Penn State College of Medicine. Fig. 2A and 4A were made by using BioRender.com.

Keyword: Oxytocin, Oxytocin receptor, Brain mapping, synaptic input, axonal output, anatomical connectivity, serial two-photon tomography, wiring diagram

Abstract

Oxytocin (OT) neurons regulate diverse physiological responses via direct connections with different neural circuits. However, the lack of comprehensive input-output wiring diagrams of OT neurons and their quantitative relationship with OT receptor (OTR) expression presents challenges to understanding circuit specific OT functions. Here, we establish a whole-brain distribution and anatomical connectivity map of OT neurons, and their relationship with OTR expression using cell type specific viral tools and high-resolution 3D mapping methods. We utilize a flatmap to describe OT neuronal expression in four hypothalamic domains including under-characterized OT neurons in the tuberal nucleus. OT neurons in the paraventricular hypothalamus (PVH) broadly project to nine functional circuits that control cognition, brain state, and somatic visceral response. In contrast, OT neurons in the supraoptic (SO) and accessory nuclei have limited central projection to a small subset of the nine circuits. Surprisingly, quantitative comparison between OT output and OTR expression showed no significant correlation across the whole brain, suggesting abundant indirect OT signaling in OTR expressing areas. Unlike output, OT neurons in both the PVH and SO receive similar mono-synaptic inputs from a subset of the nine circuits mainly in the thalamic, hypothalamic, and cerebral nuclei areas. Our results suggest that PVH-OT neurons serve as a central modulator to integrate external and internal information via largely reciprocal connection with the nine circuits while the SO-OT neurons act mainly as unidirectional OT hormonal output. In summary, our OT wiring diagram provides anatomical insights about distinct behavioral functions of OT signaling in the brain.

Significance Statement

Oxytocin (OT) neurons regulate diverse physiological functions from pro-social behavior to pain sensation via central projection in the brain. Thus, understanding detailed anatomical connectivity of OT neurons can provide insight on circuit specific roles of OT signaling in regulating different physiological functions. Here, we utilize high resolution mapping methods to describe the 3D distribution, mono-synaptic input and long-range output of OT neurons, and their relationship with OT receptor (OTR) expression across the entire mouse brain. We found OT connections with nine functional circuits controlling cognition, brain state, and somatic visceral response. Furthermore, we identified a quantitatively unmatched OT-OTR relationship, suggesting broad indirect OT signaling. Together, our comprehensive OT wiring diagram advances our understanding of circuit specific roles of OT neurons.

Introduction

Oxytocin (OT) is a highly conserved neuropeptide, playing key roles in regulating social behavior and other physiological functions (Althammer et al., 2018; Jurek and Neumann, 2018; Quintana and Guastella, 2020). Impairment in OT signaling has been heavily implicated in many neurodevelopmental disorders including autism (Francis et al., 2014; Rajamani et al., 2018). Altering OT signaling is being pursued as a potential therapy to alleviate social behavioral deficits in many brain disorders (Guastella and Hickie, 2015). However, our limited neural circuit based understanding of OT signaling in the brain hampers the development of targeted therapeutic approaches aimed at altering specific OT functions without affecting other biological pathways. A comprehensive anatomical understanding of OT neurons would enable integrated neural circuit specific studies to decipher the neural substrate of distinct OT functions.

The majority of OT producing neurons are located in the paraventricular nucleus of the hypothalamus (PVH) and the supraoptic nucleus (SO) while fewer OT neurons reside in the extended amygdala (Biag et al., 2012; Madrigal and Jurado, 2021). OT neurons receive input from distinct brain regions (e.g., the thalamus) and integrate sensory input with internal information to release OT in a context dependent manner in order to modulate specific downstream circuitry (Grinevich and Neumann, 2020; Tang et al., 2020). The actions of OT are mainly mediated by a single subtype of the OT receptor (OTR) expressed in distinct brain regions as well as peripheral tissues (Gimpl and Fahrenholz, 2001; Grinevich et al., 2016; Newmaster et al., 2020). In addition to the well-known peripheral release of OT as a hormone via the posterior pituitary, OT neurons send direct projections to specific brain areas that frequently express OTR, thereby modulating circuit specific functions (Grinevich et al., 2016; Liao et al., 2020). For example, OT signaling is linked with the medial prefrontal cortex for social cognition (Sabihi et al., 2014; Li et al., 2016), CA2 of the hippocampus for social memory (Raam et al., 2017; Tirko et al., 2018), the central amygdala for fear modulations (Knobloch et al., 2012; Ferretti et al., 2019), the parabrachial nucleus (PB) for fluid intake (Ryan et al., 2017), and the spinal cord for pain perception (Eliava et al., 2016; Boll et al., 2018). Despite these prior studies, we still lack a quantitative and comprehensive wiring diagram of the OT neurons in a standard 3D reference brain.

Here, we establish a comprehensive wiring diagram of OT neurons in the mouse brain using a high-resolution quantitative brain mapping method in combination with cell type specific transgenic mice and viral tools. All whole brain datasets are registered in the Allen Common Coordinate Framework (CCF) to facilitate data cross-comparison (Wang et al., 2020), and high resolution images can be easily viewed using a new web visualization (https://kimlab.io/brain-map/ot_wiring/). Using the new resource, we identified distinct OT neuronal connection with nine circuits that can explain diverse OT functions. Moreover, we found lack of quantitative correlation between OT output and OTR expression across the whole brain, suggesting abundant indirect OT signaling in OTR expressing brain areas.

Material and Method

Animals

All animal care and experimental procedures are approved by the Penn State University Institutional Animal Care Use Committee (IACUC). *Ot-Cre* mice (Choe et al., 2015) were originally produced in the Gloria B. Choi lab at the Massachusetts Institute of Technology and imported to the Penn State University (Kim Lab). To generate OT-Cre;Ai14 mice, *Ot-Cre* mice were crossed with Ai14 mice, expressing tdTomato following Cre-mediated recombination (Jax: 007914, C57Bl/6 J background). 2 months old C57Bl/6 J mice were used for whole brain tissue clearing and immunostaining. Mice received food and water ad libitum and were housed under constant temperature and light conditions (12 hrs light and 12 hrs dark cycle).

Experimental design and statistical analyses

For OT neuron distribution mapping (Fig.1), we used 3 males, 3 females (virgin), and 2 females (lactating) of 2 – 4 month old OT-Cre;Ai14 mice with STPT imaging. We also used 4 males, 3 females (virgin) of 2 month old C57bl/6 mice for tissue clearing and LSFM imaging based quantification (Fig.1). Since we did not observe significant difference in OT neuronal number, we combined data from both sexes to generate representative cell counting (Table 1). For anterograde projectome mapping in 2 – 4 month old OT-Cre (Fig.2), we used 2 males, 3 females (virgin), and 3 females (lactating) with 500nl of AAV injection, and 3 males, 3 females (virgin), and 1 female (lactating) with 50-150nl of AAV injection for the PVH targeting. Moreover, we used 5 males and 5 females (virgin) for the SO, 3 males and 2 females (virgin) for the TU, 1 male and 1 female (virgin) for the AN. For oxytocin receptor expression mapping using OTR-Venus mice (Fig.3), we used 6 males and 8 females (virgin). For rabies input mapping (Fig.4), we used 3 males and 3 females (virgin) for the PVH, and 3 males and 1 female (virgin) for the SO.

To determine the correlation between OT area normalized projection and OTR density (Fig. 3C), we first tested for the normality of the data using the D'Agostino-Pearson normality test. Based on the normality test result, we performed Spearman nonparametric correlation test. GraphPad Prism 8 was used for all statistical analysis and graphs.

Stereotaxic surgery and virus injections

Ot-Cre mice (8-11 weeks old, males and females) were anesthetized with isoflurane (controlled with Somnosuite, Kent Scientific) and mounted on a stereotaxic instrument (Angle Two, Leica) with a heating pad placed underneath. All injections were performed with pulled micropipettes (VWR, Cat# 53432-706). Through the small opening of the micropipette, virus was delivered at a rate of 75-100 nL per minute. The speed and volume of injection were monitored along with the calibration marks on the micropipette (1 mm =100 nL). To target the PVH, coordinates are anteroposterior (AP) from the Bregma: -0.58 mm; mediolateral (ML): 0.27 mm; dorsoventral (DV): -4.75 mm. Anterior PVH and posterior PVH injection coordinates are -0.35 mm (AP), 0.3 mm (ML), and -4.5 mm (DV) and -0.94 mm (AP), 0.39 mm (ML), and -4.55 mm (DV), respectively. Coordinates for the SO are -0.66 mm (AP), 1.3 mm (ML), and -5.8 mm (DV). For anterograde tracing, 50-500 nL of AAV2-CAG-Flex-EGFP virus (titer 3.7 x 10^{12} vg/ml, purchased from UNC vector core) was injected into the PVH (500 nL for maximum coverage, 50-150 nL for PVH subregion) and 150 nL of the virus was injected into the SO. Mice were

euthanized three weeks later with Ketamine (100 mg/kg) and Xylazine (10 mg/kg) mixture. For monosynaptic retrograde labeling, 50-500 nL of rAAV1-synp-DIO-STPEPB (titer 3.9 x 10^{12} cg/ml, purchased from UNC vector core, a gift from Ian Wickersham (Addgene plasmid # 52473 ; http://n2t.net/addgene:52473 ; RRID:Addgene_52473 (Kohara et al., 2014)) was injected into the PVH, followed by the same quantity of EnvA G-deleted Rabies-mcherry virus (titer: 8.12x10^{8} TU /ml, purchased from the Salk Institute Viral Vector Core, a gift from Edward Callaway (Osakada et al., 2011), RRID:Addgene_32636) three weeks later into the same location. Mice were euthanized 7-8 days later with Ketamine (100 mg/kg) and Xylazine (10 mg/kg) mixture.

Control experiments were performed by injecting 500nl of rAAV1/Synp-DIO-STPE (titer 4.3 x 10^{12} vg/ml, purchased from UNC vector core, a gift from Ian Wickersham (Addgene plasmid # 52474 ; http://n2t.net/addgene:52474 ; RRID:Addgene_52474) (Kohara et al., 2014)) in *Ot-Cre* mice at the same co-ordinates for PVH and SO (N=1 each). EnvA G-deleted Rabies-mcherry virus was injected 3 weeks later and the mice were euthanized 7 days later for brain collection.

To check for leakiness of TVA, 500nl of rAAV1-synp-DIO-STPEPB was injected along with 50ul of 1:4 diluted pAAV-CAG-tdTomato (codon diversified) (a gift from Edward Boyden (Addgene plasmid # 59462 ; http://n2t.net/addgene:59462 ; RRID:Addgene_59462) in C57 mice at the same co-ordinates for PVH.

For the optimized G and split TVA tracing, AAV5-CAG(del)>TCIT(-ATG)-Flex(*loxP*)-SV40 (1:8 dilution, titer: 1.6 E+12gc/ml, a gift from Todd Anthony at Harvard) was co-injected with AAV5- CAG(del)>nC2oG-Flex(loxP) (titer: 2.8 E+12gc/ml, a gift from Todd Anthony) in *Ot-Cre* mice (N=2 each for PVH and SO co-ordinates) (150nl per brain). After 14 days, the same volume of EnvA G-deleted Rabies-EGFP virus (titer:4.89E+09 TU/ml, purchased from Salk Institute viral vector core, a gift from Edward Callaway (Addgene plasmid # 32635 ; http://n2t.net/addgene:32635 ; RRID:Addgene_32635) (Osakada et al., 2011)) was injected into the same location. The mice were euthanized 7 days later for brain collection and STPT imaging.

STPT imaging and related data analysis

Transgenic or virus injected mice were transcardially perfused with 4% paraformaldehyde (PFA) in 0.1M phosphate buffer (PB, pH 7.4) after 0.9% saline. Brains were dissected out and post-fixed in 4% PFA overnight at 4°C. Fixed brains were stored in 0.05 M phosphate buffer at 4°C until imaged. To image the entire brain, serial two-photon tomography (TissueCyte 1000; Tissuevision) was used as previously described (Ragan et al., 2012; Kim et al., 2017; Newmaster et al., 2020). Briefly, the brain was embedded in 4% oxidized agarose and cross-linked with 0.2% sodium borohydride solution. The brain was imaged as 12 x 16 x 280 tiles with 1 x 1 μm^2 *x,y* pixel resolution in every 50 µm *z*-section. We used 910 nm wavelength for two-photon excitation to excite both green (e.g., eGFP) and red signals (e.g., tdTomato). Signals were separated with 560 nm dichroic mirror and two band path filters (607/70-25 for red and 520/35-25 for green). Imaging tiles in each channel were stitched with custom-built software (Kim et al., 2017; Newmaster et al., 2020).

For quantitative projection data analysis, we used our previously published pipeline (Jeong et al., 2016). Briefly, both signal and background channels were z-normalized. Then, the background channel images were subtracted from the signal channel images to increase signal-to-noise ratio.

Then, projection signals were converted to a binary map by applying an optimized threshold (8x standard deviation) to detect signals while minimizing noise from background autofluorescence. Then, binarized signals in each pixel were counted in 20 x 20 (*x,y*) pixel unit (voxel) and the value was assigned the corresponding voxel across the brain, which is defined as "projection strength". Thus, range of the projection strength in a given voxel is between 0 and 400. Projection strength of each area is calculated by summing up all projection strength within an anatomically defined area. Autofluorescence of brains was used to register each brain to the Allen CCF using Elastix (Klein et al., 2010), then, the projection signals were transformed to the reference brain. Then, we used maximum projection of registered long-range output datasets from each area to create a representative projection data for further quantitative analysis (Movie S2). "Area normalized projection" represents normalized occupancy of projection signals in the ROI by dividing the projection strength with a total number of voxels in each ROI. For example, if total voxel count for one ROI was 20,000 and our projection strength showed 2,000 in the ROI, it will be (2,000/20,000)*100 = 10%. Regions with a projection strength greater than 1% is designated as dense, between 1 and 0.5 as intermediate, between 0.5 and 0.1 as sparse, and less than 0.1 as very sparse (Fig. 2E).

For cell counting analysis, we used a machine-learning algorithm to detect fluorescently labeled cells (Kim et al., 2017; Newmaster et al., 2020). The cell density in 2D (count/mm^2) was calculated by dividing cell number with ROI area. 2D counting numbers were also converted into 3D counting using our previously calculated 3D conversion factor (1.4 for tdTomato) (Kim et al., 2017). To measure the volume of anatomical ROI, the reference Allen CCF was reverse registered onto individual brains using the Elastix. "Cell density (counts/mm^3)" was calculated by dividing detected cell numbers in 3D with the anatomical ROI volume. The cell counting analysis was applied to OT-Cre;Ai14 and OTR-Venus cell distribution and inputs to the OT neurons. We used an average of individual datasets to create representative OT (OT-Cre;Ai14, Movie S1) and OTR (OTR-Venus, Movie S3) distribution and maximum projections to create mono synaptic input for OT neurons (rabies). For rabies input degree (Fig. 4D, Movie S4), Regions more than 100 cells are designated as dense, between 100 and 10 as intermediate, and less than 10 as sparse.

To compare relative abundance between OT output and OTR expression in Fig. 3C., relative cell density or output data in each region was calculated by dividing each data by summed density or output data from all areas (excluding viral injection sites), respectively. Then, log10 (relative OT output/relative OTR) was used to examine the quantitative relationship between the two signals.

2D hypothalamic and PVH Flatmap

To generate the hypothalamic flatmap, we adapted the previously used method (Kim et al., 2017) and applied it to the hypothalamic region. First, we created a binary image in the hypothalamic area based on the oxytocin expression. Second, a zero line was placed to generate evenly spaced bins along the dorsal to the ventral direction of the PVH and laterally extended to include TU and MEA at different coronal plains. To capture signals on the flatmap, bins were registered into the reference brain and the cell number in each bin was quantified as described before in the STPT data analyses section. Lastly, the mean number of the OT neurons in 8 OT-Cre;Ai14 brains were plotted in each flatmap using a custom-built matlab code. For the PVH flatmap, we followed the same procedure to generate a hypothalamic flatmap except for bin generation. Instead of delineating bins in a binary image, we assigned bin numbers in the PVH subregion of Franklin-Paxinos atlas (Paxinos and Franklin, 2008) in the dorsal to the ventral direction.

240

241 Whole brain clearing and immunostaining, light sheet microscopy, and cell counting

242 C57Bl/6 J mice (4 males and 3 females at P56) were transcardially perfused with 0.9% saline
243 followed by 4% PFA in 0.1M phosphate buffer (PB, pH 7.4). The decapitated heads were
244 postfixed in 4% PFA overnight at 4°C and brains were dissected out the following day. All the
245 following steps were performed on an orbital shaker unless otherwise specified. Dissected brains
246 were delipidated in SBiP buffer (0.2mM Na_2HPO_4, 0.08% SDS (Sodium Dodecyl Sulfate),
247 0.16% 2-methyl 2-butanol, 0.08% 2-propanol). Delipidation was performed with 3-4 washes
248 (10ml per wash) in SBiP for 24 hrs followed by one 10ml wash with SBiP for the next 4 days.
249 Samples were then moved to B1n buffer (0.1%v/v Tritox-X-100, 1% wt/v glycine, 0.001N
250 NaOH, 0.008% wt/v sodium azide) for 1 day (10ml) and then shifted to 37^0C incubation for 3
251 hrs. Once delipidation was completed, the samples were washed in PTwH (Tween 20- 2ml,
252 10mg/ml Heparin- 1ml and sodium azide-2g, made to 1L with 0.1M phosphate buffered saline)
253 3-5 times at 37^0C for 24 hrs. The samples were then incubated in antibody solution (5% DMSO
254 and 3% Donkey serum in PTwH- 4ml per sample) containing primary antibodies for OT
255 (ImmunoStar Cat# 20068, RRID:AB_572258, 1:500) and Vasopressin (Peninsula Laboratories
256 Cat#T-5048, RRID:AB_2313978, 1:1000) for 10 days at 37^0C. Next, PTwH washes were
257 performed 4-5 times for 24 hrs at 37^0C, followed by secondary antibody incubation. Secondary
258 antibodies (1:500) were used as follows: Alexa Fluor 594 AffiniPure Fab Fragment Donkey
259 Anti-Rabbit IgG (H+L) (Cat # 711-587-003, RRID: AB_2340623) and Alexa Fluor 647
260 AffiniPure $F(ab')_2$ Fragment Donkey Anti-Guinea Pig IgG (H+L) (Cat # 706-606-148,
261 RRID:AB_2340477) in antibody solution (4ml per sample) for 10 days at 37^0C. The samples
262 were further washed 3-4 times in PTwH for 24 hrs at 37^0C. Once immunolabeling was
263 completed, the samples were moved to room temperature (RT) and further processed for tissue
264 clearing. All the following steps were performed in a fume hood in glass containers and the
265 containers were filled completely. Samples were dehydrated in the following series of methanol
266 dilutions: 20%v/v -1 hr at RT, 40%v/v- 1 hr at RT, 60%v/v- 1 hr at RT, 80%v/v- 1 hr at RT,
267 100%v/v - 1 hr at RT and 100%v/v at RT overnight. Next, the samples were incubated for 3 hrs
268 in 66%v/v dichloromethane/33%v/v Methanol at RT followed by 100% dichloromethane (Sigma
269 Cat# 270997) incubations of 30min and 2hrs. Samples were then index matched in benzyl ether
270 (Sigma Cat#108014) overnight without shaking. Once the samples are completely transparent (1-
271 2 days), samples were moved to ethyl cinnamate (Sigma Cat#112372). Whole brain samples
272 were then imaged using a light sheet microscope (SmartSPIM, Life Canvas) at 4x resolution.

273 OT cell detection and 3D counting workflow are similar to the STPT based quantification by
274 applying a 2-D FFT high pass filter, normalizing the data by dividing it by the filtered part,
275 thresholding and 3D water-shedding to find the mask of each cell, and finally documenting each
276 cell with its centroid location.
277

278 Immunohistochemistry, microscopic image, and cell counting

279 For immunohistochemistry, fixed brains were either embedded in 3% agarose or frozen after
280 sinking in 30% sucrose in 0.2 M Phosphate buffer. Embedded or frozen brains were then cut on a
281 vibratome (Leica vt1000s) or a microtome (Leica SM2010 R) at 50 µm thickness. Sections were
282 stored at −20°C in a cryoprotectant solution (30% sucrose and 30% glycerol in 0.1 M PB) until
283 immunostaining. For oxytocin staining, sections were washed three times in 1x PBS. After 1

hour incubation in blocking solution (10% donkey serum and 0.1 % Triton X-100), slices were incubated with oxytocin primary antibody (ImmunoStar Cat# 20068, RRID:AB_572258, 1:1000) in blocking solution for overnight at 4 °C. Sections were then washed three times with 1x PBS and further incubated in secondary antibodies (Thermo Fisher Scientific Cat# A-21206, RRID:AB_2535792, 1:500) for 1 hour at room temperature. After washing three times, slices were mounted onto slides and coverslipped with vectashield mounting media (Vector laboratories, H-1500-10). For microscopic imaging, a BZ-X700 fluorescence microscope (Keyence) and a confocal microscope (Zeiss 510) were used. A low magnification objective lens (4x) was used to image with a large enough view to define brain anterior-posterior location from bregma and higher magnification objective lenses (10x ~ 40x) were used to image sections depending on the cell density. Images were delineated manually based on the Franklin-Paxinos atlas and fluorescently tagged cells were manually quantified using the cell counter plug-in in FIJI (ImageJ, NIH).

Software Accessibility

All custom-built codes and flatmaps used in the current study will be freely available upon request and can be used without any restriction.

Data Sharing Plan

Data files for the anterograde projectome, rabies based monosynaptic input, and OTR expression data registered on the Allen CCF are included as supplementary data.

High-resolution serial two-photon tomography images will be deposited in BrainImageLibrary (https://www.brainimagelibrary.org/) and web visualization link will be added upon publication.

Results

Quantitative density mapping of oxytocin neurons reveals four clusters in the adult mouse brain

We first aim to determine quantitative brain-wide OT distribution in complex 3D structures. To examine the anatomical distribution of OT neurons across the whole brain, we used OT knock-in mice with Cre recombinase (*Ot-Cre*) crossed with Ai14 reporter mice (OT-Cre;Ai14-heterozygotes) (Choe et al., 2015). We imaged the entire mouse brain at cellular resolution using serial two-photon tomography (STPT) and performed quantitative mapping using previously established computational methods (n=8 brains, Fig. 1A-B, Movie S1) (Kim et al., 2017). The PVH regions (PVH, descending division of PVH, anterior, intermediate, and subparaventricular zone) contain the highest density of OT neurons (~39%, 742 out of total 1899 cells) followed by the tuberal nucleus (TU), SO, and other areas (Table 1). To further visualize the spatial expression pattern of OT neurons, we created a flatmap (Fig. 1C). Evenly spaced bins provide a flattened 2D spatial unit to quantify and to display signals from the 3D brain. The flatmap was delineated with Allen Common Coordinate Framework (Allen CCF) and Franklin-Paxinos atlas based anatomical labels (Fig. 1C-D) (Paxinos and Franklin, 2008; Chon et al., 2019; Wang et al., 2020). The regional boundaries of the two labeling systems generally agreed with each other in the major OT expressing regions (e.g., the PVH and the SO) despite noticeable discrepancies in the caudal hypothalamic area (e.g., the TU) (Fig. 1C-D) (Chon et al., 2019). The OT density heatmap on the hypothalamic flatmap clearly shows four clusters: 1. the PVH, 2. the SO, 3. accessory nuclei (AN), 4. the TU area (Fig. 1E) (Knobloch and Grinevich, 2014). Notably, the largely overlooked TU area contains almost as high density of OT neurons as the PVH area (Fig. 1E).

To distinguish neurons actively expressing OT in adults from developmentally labeled cells, we performed immunohistochemistry using an OT antibody in OT-Cre;Ai14 mice. We confirmed that almost all OT immuno positive neurons (97%, 1733 out of 1790 cells, n=4 animals) were labeled by tdTomato from OT-Cre;Ai14 mice (Fig. S1). In contrast, 76% of tdTomato labeled cells were OT immuno positive (1733 out of 2277 cells) in the PVH. Smaller portions of tdTomato cells in the SO (44%, 654 out of 1508 cells) and the MEA (8%, 31 out of 375 cells) retain active OT expression (Fig. S1). This result suggested that OT neurons undergo OT expression changes during neurodevelopmental processes (Madrigal and Jurado, 2021).

To cross validate active expression of OT in the adult brain, we performed tissue clearing followed by 3D immunolabeling with OT and vasopressin antibodies in 8 weeks old C57bl/6 mice (n= 7 brains; Fig. 1F-I) (Renier et al., 2016). We developed 3D counting and image-registration methods to achieve similar unbiased brain-wide cell counting as done with STPT imaging (see Methods for more details). We observed similar OT staining distribution and overall slightly higher counting compared to our transgenic based mapping results (Table 1). For example, the estimated number of OT neurons in the PVH with the immunostaining was 1,095 cells out of total 3149 cells (~35%), which is higher than our transgenic based estimate mostly likely due to sensitive labeling based on antibody detection. Importantly, we confirmed the robust OT expression in the TU area that was not colocalized with vasopressin staining (Fig. 1I).

Quantitative whole brain projection mapping of OT neurons reveals broad long-range projections in nine functional circuits

Next, we aim to establish a comprehensive anterograde projection map from OT neurons in the four identified areas and examine whether OT projections target specific functional circuits related to distinct behavior control.

Since OT can be released via axons, dendrites, and even neuronal processes (Jurek and Neumann, 2018), we injected a Cre-dependent adeno associated virus 2 (AAV2-CAG-Flex-EGFP) in the four areas of *Ot-Cre* knock-in mice with slightly varying injection sites to cover target areas (N = 15 animals for the PVH, 10 for the SO, 2 for the AN, and 5 for the TU) (Fig. 2A-B). We included male, virgin female, and lactating female mice in our study (see method for more detail), and observed no significant difference between sex or lactating state. Thus, we merged all data from the same anatomical areas. Long-range projection signals from individual injections were then registered onto the Allen CCF and maximum projection data in all samples from each anatomical area were used to represent efferent output for the four areas (Fig. 2C; Movie S2). We found abundant projections from OT neurons in the PVH to the midbrain and hindbrain areas while relatively sparse projection to the diencephalon and telencephalon areas (Fig. 2D)

We then examined whether OT neurons in the four anatomical areas show any distinct projection pattern. Overall, the PVH neurons showed the broadest projection pattern followed by the SO and the AN, which project to a small subset of PVH-OT efferent areas (Fig. 2D-E; Movie S2). The TU-OT neurons did not show any long-range projections. We ask whether OT neurons project to distinct neural circuits related to specific function. Based on known functions of each anatomical region, we found that PVH-OT neurons project to three functional modules that control the internal state, somatic visceral, and cognitive response. Each module contains three circuits. The internal state module contains attention, threat/alert/defense, and sleep/awake circuits (Fig. 2E). The somatic visceral module includes pain, sensory motor, and body physiology/metabolism circuits (Fig. 2E). Lastly, the cognitive control module has learning/memory, reward/value assessment, and reproduction circuits (Fig. 2E). Each circuit is composed of multiple brain regions from the hindbrain, midbrain, thalamus, hypothalamus, cerebral nuclei, and cerebral cortex that process low-to-high order information. For instance, many basal ganglia circuit components including the caudate putamen (CP), globus pallidus (GP), subthalamic nucleus (STN), and substantia nigra (SN) receive OT projection to modulate motor function (see sensory motor regulation in Fig. 2E). PVH-OT neurons project to these areas at varying degrees. Dense projection occurs largely onto the hindbrain (e.g., the dorsal motor nucleus of the vagus nerve; DMX, the parabrachial nucleus; PB), the midbrain (the substantia nigra compacta; SNc), and the hypothalamus (the medial preoptic nucleus; MPN) to directly modulate motor output and sensory input (Fig. 2E). In contrast, the cerebrum (the cerebral nuclei and cerebral cortex) that works as high cognitive controller receives more sparse projection (Fig. 2E). The SO and AN project to a small subset of PVH-OT target areas (Fig. 2E). This data suggests that OT neurons in these two areas can further modulate a subset of the nine functional circuits, albeit less powerfully.

Together, our comprehensive projectome analysis uncovers anatomical substrates to explain pleiotropic effect of OT neurons regulating diverse behavioral outcomes.

Oxytocin receptor expression showed quantitative mismatch with oxytocin neuronal output

Next, we ask whether expression of a single subtype of the OT receptor (OTR) is quantitively correlated with OT projection target areas to mediate circuit specific OT function. Although most

OT projecting areas are known to contain OTR expression (Grinevich et al., 2016), the quantitative relationship between OT projection and OTR expression across the whole brain is currently lacking.

To understand OT-OTR correlation, max OT projectome data from both the PVH and SO were compared to OTR expression in adult mice using a previously validated mouse line, OTR-Venus (Newmaster et al., 2020). A cohort of adult OTR-Venus mice brains were imaged using STPT and mapped OTR expression in the whole adult brain. These mapped OTR positive neurons (magenta in Fig. 3A) were registered onto the same reference brain along with OT-projections (green in Fig. 3A). Overall, the OTR showed high expression in the cortical area with minimal OT projection, while many midbrain and hindbrain regions have strong OT with little OTR expression (Fig. 3A-B; Movie S3). When we examined whether relative projection of OT neurons is correlated with relative OTR density across the entire brain, we found no significant correlation across the whole brain and major brain areas, except for the thalamus and the medulla (Fig. 3C). Overall, our results highlight lack of quantitative and spatial correlation between OT projections and OTR expression in the mouse brain.

Then, how do OTR rich areas (e.g., the isocortex) receive OT signaling without direct OT projection? A previous study suggested that many OTR expressing neurons may receive OT signal non-synaptically via cerebral spinal fluid (CSF) (Zheng et al., 2014). Hence, we examined whether OT projection fibers make physical contact with ventricles. Indeed, we frequently found OT fibers with thick varicosities at the lateral, 3rd, and 4th ventricle surface (Fig. 3D). This further suggests that OT signaling may transmit to the brain via the CSF route in addition to direct transmission in target areas.

OT neurons mainly receive monosynaptic inputs from the thalamus, hypothalamus, and cerebral nuclei.

Since OT neurons are known to integrate external stimuli and internal state, we ask whether OT neurons in the PVH and the SO receive mono-synaptic input from sensory and integrative information processing brain areas.

To map brain-wide mono-synaptic inputs in a cell type specific manner, conditional retrograde pseudorabies viruses were injected into the PVH and the SO of the *Ot-Cre* knock-in mice separately (Fig. 4A) (Wickersham et al., 2007). We confirmed the specificity of labeling by performing co-immunolabeling TVA positive neurons with OT and AVP. None of the TVA infected neurons were AVP positive and were largely OT positive (Fig. S2). We also confirmed no leakiness of TVA labeling by injecting TVA in the PVH of adult C57 mice which did not result in any infection (Fig. S2). To confirm G protein dependency for monosynaptic tracing, TVA without G and rabies viruses were injected to the PVH and SO separately and the brains were imaged in STPT (N=1 animal each for the PVH and SO). All the neurons observed were confined to the injection site and both samples were devoid of any long-range input cells. Lastly, we performed another rabies tracing experiment with optimized G and split TVA that are known for improved Cre specificity and tracing (Kim et al., 2016). We found near identical results with this alternative virus approach (Fig. S3) (N=2 animals, each for the PVH and SO). Once we confirmed the validity of our input tracing methods, we used our mapping method to quantify input neurons throughout the whole brain (Kim et al., 2017). To acquire overall inputs to each anatomical area, input signals from multiple independent injections targeting a specific brain region were registered

onto the Allen CCF and the max projection of input signals from each anatomical area (N = 6 animals for the PVH and 4 for the SO) were overlaid onto the reference brain (pseudo-colored green for the PVH and magenta for the SO in Fig. 4B-C; Movie S4).

Overall, OT neurons from the PVH mainly receive inputs from the thalamus, hypothalamus, and cerebral nuclei (Fig. 4C). All brain regions providing inputs to the OT neurons also receive output from the OT neurons except the triangular nucleus of septum (TRS), creating reciprocal connections with afferent areas (Fig. 2E and 4D). Noticeably, OT neurons received little input from hindbrain despite strong output to the same area, suggesting that OT neurons provide largely unilateral output to the hindbrain (Fig. 2E and 4D). Moreover, the cerebral cortex provides little to no input to the OT neurons, further supporting very weak direct interaction between cerebral cortical areas and OT neurons (Fig. 4D; Movie S4).

SO-OT neurons receive overall similar input compared to the PVH-OT neurons (Fig. 4D). The broad afferent pattern is in sharp contrast to the very sparse efferent projection of SO-OT neurons to the brain (Fig. 2E and 4D). When monosynaptic input from the PVH- and SO-OT neurons are compared, SO-OT neurons show input from relatively more lateral parts of the brain (Fig. 4C, arrows).

Collectively, we conclude that OT neurons in the PVH and the SO receive similar input from a subset of brain areas that receive majority of input from hypothalamic areas followed by cerebral nuclei and thalamic areas. (Fig. 4D).

Input-output wiring diagrams of PVH- and SO-OT neurons provide overall neural circuit control patterns.

Based on our long-range output and mono-synaptic input data, we constructed input-output circuit diagrams of OT neurons in the PVH and the SO while annotating each brain area based on their functional categories (Fig. 5). PVH-OT neurons project broadly to all nine identified functional circuits throughout the brain, indicating that OT neurons can modulate information processing at different level of circuits with overall stronger influence in the mid- and hindbrain circuits (Fig. 5). In contrast, mid-level circuits including the diencephalon (the thalamus, hypothalamus), the midbrain, and the cerebral nuclei, provide major input to inform action of OT neurons, providing anatomical substrate to perform an integrative role (Fig. 5). SO-OT neurons receive similar mid-level circuit input compared to the PVH-OT neurons while showing limited central projection to the midbrain and pons (Fig. 5). This suggests that SO-OT neurons mainly serve as peripheral hormonal output.

Discussion

The wiring diagram of the brain is a structural foundation to decipher neural circuits underlying brain function. Here, we present a comprehensive anatomical connectivity map of the hypothalamic OT neurons and their relationship with postsynaptic OTR expression in the whole mouse brain. A quantitative mismatch exists between OT projection and OTR distribution pointing towards abundant non-synaptic OT signaling within the brain. We also identify nine functional circuits with reciprocal or unidirectional connection with OT neurons that serve as anatomical entities to exert varied behavioral control.

OT neurons are mostly located in hypothalamic nuclei with a complex 3D shape (Biag et al., 2012; Madrigal and Jurado, 2021). To examine OT expression intuitively and quantitatively, we devised a 2D flatmap for OT containing hypothalamic regions from an Allen CCF based reference brain while incorporating anatomical labels from the Allen Institute and Franklin-Paxinos (Paxinos and Franklin, 2008; Wang et al., 2020). This approach allows for the interpretation of OT anatomical location from two independently created and commonly used atlases (Chon et al., 2019) and provides an alternative coordinate system to understand anatomical connectivity. In addition to well-described OT neurons in the PVH, SO, and AN, we described another major population in the TU area in the hypothalamus (Jirikowski, 2019). Our 3D immunolabeling independently validated the existence of this extra population. Our anterograde tracing showed that these neurons have almost no central projection, suggesting their contribution to brain information processing is limited. Future studies including ablation studies will help to elucidate the functional significance of this overlooked OT population.

OT signaling is known to modulate many distinct brain functions such as anxiolytic effect, social memory, and attention (Lee et al., 2009; Marlin et al., 2015; Grinevich and Stoop, 2018; Schiavo et al., 2020). By extensively mapping OT efferent processes and clustering brain regions based on known functions, we identified nine functional circuits where OT processes interact to modulate distinct behavioral circuits. Each circuit consists of a set of brain regions processing different behavioral aspects. Thus, our circuit map can help to understand neural entities of OT that modulate different behavioral aspects. Overall, OT circuits provide broad projections to modulate external and internal information throughout the entire brain circuit. For example, we found that OT neurons project to sensory-motor and pain circuits from the hindbrain and midbrain to cerebral cortex and cerebral nuclei. A recent single cell reconstruction study demonstrated that even a single magnocellular OT neuron can make multiple collateral projections to extra-hypothalamic areas to coordinate neuromodulation across functionally related brain circuits (Zhang et al., 2020). These provide anatomical evidence that OT neurons can finely modulate sensory motor processing throughout different circuit levels. Notably, OT neurons project to other neuromodulatory areas such as the locus coeruleus for norepinephrine (alert), the substantia nigra (movement) and the ventral tegmental areas for dopamine (reward), and raphe nuclei for serotonin (emotion), thus serving as a master neuromodulator of neuromodulations (Yoshida et al., 2009; Dölen et al., 2013; Hung et al., 2017; Froemke and Young, 2021). The most well-established role of OT signaling is to promote social behavior (Kemp and Guastella, 2010; Shamay-Tsoory and Abu-Akel, 2015). Social behavior is a complex behavior, requiring coordinated interplay between the sensory system and integrative circuits to generate socially appropriate motor outputs. Extensive connections of OT neurons to somatic visceral, cognitive, and state control modules can help to fine-tune activity of different circuit components to generate enhanced response to socially salient stimuli.

OT gets released through axonal and dendritic projections based on the inputs that OT neurons receive. The presence of large dense core vesicles containing OT at the non-active zones of pre-synapses (Theodosis, 1985; Griffin et al., 2010), absence of evidence for OTR in the postsynaptic membranes, and extremely delayed electrophysiological OT response (milliseconds to seconds) (Knobloch et al., 2012; Knobloch and Grinevich, 2014) collectively support non-synaptic axo-dendritic release of OT. Hence, our projection maps with entire process labeling provide possible release sites of OT throughout the whole brain. We also compared OT total projections (combined data from the PVH- and SO-OT neurons) to OTR expression in the central brain. Although earlier studies mentioned OT-OTR discrepancy, recent studies showed that most OTR expressing areas contain at least sparse OT projection (Knobloch et al., 2012; Grinevich et al., 2016; Mitre et al., 2016; Zhang et al., 2020). Despite a few areas with high levels of both OTR and OT projection (e.g., the paraventricular thalamus), our analysis revealed no significant quantitative correlation between OT and OTR across entire brain regions. For example, the cerebral cortical area contains abundant OTR with little to no OT axons. However, OT can still mediate sensory stimuli in the cortex to modify mouse behavior (Marlin et al., 2015; Schiavo et al., 2020). Previous studies suggest that OTR neurons in the isocortex may receive OT signals indirectly from ventricular pathways via cerebral spinal fluid with delayed and long-lasting effects (Mens et al., 1983; Zheng et al., 2014). Indeed, we found that long-range processes from OT neurons contact the ventricle surface, suggesting potential release of OT into the CSF via long-range processes. Another noteworthy OT-OTR discrepancy is brain regions with abundant OT projection without OTR expression such as sensory related hindbrain areas. Although OTR is a main OT receptor, OT can bind to another receptor to exert its effect. For example, OT can elicit TRPV1 activity in the spinal cord to modulate nociception (Nersesyan et al., 2017). OT modulation in the central nervous system through these non-canonical pathways are under explored and requires further study.

Our OT mono-synaptic input maps showed that the majority of inputs are from the cerebral nuclei, thalamus, hypothalamus, and midbrain with little input from the hindbrain. Particularly, almost all afferent brain regions to PVH-OT neurons also receive efferent projections, suggesting strong reciprocal control of target regions by PVH-OT neurons except the hindbrain for unidirectional output. Abundant bidirectional connections with nine functional circuits suggest that PVH-OT neurons can be an allostatic tool to interactively orchestrate and facilitate social and non-social information processing based on external stimuli and internal state (Quintana and Guastella, 2020). In contrast, despite having similar afferent areas to SO-OT neurons, their limited central projection suggest that SO-OT neurons serve largely as unidirectional hormonal output to the periphery rather than reciprocal circuit modulator.

In summary, our study provides an anatomical foundation to understand diverse functions based on OT neurons in the brain. We deposit all high-resolution imaging data in publicly accessible databases and our website to facilitate data mining. We envision that this OT wiring diagram with quantitative expression data will guide future studies to understand circuit-based mechanisms of OT function and its changes in socially relevant behaviors as well as brain disorders such as autism.

561

562 **Contributions**

563 Conceptualization, Y.K.; Data Collection and analysis, S.S., S.M., K.N., M.C., Y.K.; Computer
564 Coding, Y.W.; Web visualization, D.J.V., K.C.; Virus making, T.A.,; Manuscript preparation:
565 S.S., S.M., Y.K with help from the other authors.

566

567

References

Althammer F, Jirikowski G, Grinevich V (2018) The oxytocin system of mice and men-Similarities and discrepancies of oxytocinergic modulation in rodents and primates. Peptides 109:1–8.

Biag J, Huang Y, Gou L, Hintiryan H, Askarinam A, Hahn JD, Toga AW, Dong HW (2012) Cyto- and chemoarchitecture of the hypothalamic paraventricular nucleus in the C57BL/6J male mouse: A study of immunostaining and multiple fluorescent tract tracing. Journal of Comparative Neurology 520:6–33.

Boll S, Almeida de Minas AC, Raftogianni A, Herpertz SC, Grinevich V (2018) Oxytocin and Pain Perception: From Animal Models to Human Research. Neuroscience 387:149–161.

Choe HK, Reed MD, Benavidez N, Montgomery D, Soares N, Yim YS, Choi GB (2015) Oxytocin Mediates Entrainment of Sensory Stimuli to Social Cues of Opposing Valence. Neuron 87:152–163.

Chon U, Vanselow DJ, Cheng KC, Kim Y (2019) Enhanced and unified anatomical labeling for a common mouse brain atlas. Nature communications 10:5067.

Dölen G, Darvishzadeh A, Huang KW, Malenka RC (2013) Social reward requires coordinated activity of nucleus accumbens oxytocin and serotonin. Nature 501:179–184.

Eliava M et al. (2016) A New Population of Parvocellular Oxytocin Neurons Controlling Magnocellular Neuron Activity and Inflammatory Pain Processing. Neuron 89:1291–1304.

Ferretti V, Maltese F, Contarini G, Nigro M, Bonavia A, Huang H, Gigliucci V, Morelli G, Scheggia D, Managò F, Castellani G, Lefevre A, Cancedda L, Chini B, Grinevich V, Papaleo F (2019) Oxytocin Signaling in the Central Amygdala Modulates Emotion Discrimination in Mice. Current biology : CB 29:1938--1953.e6.

Francis SM, Sagar A, Levin-Decanini T, Liu W, Carter CS, Jacob S (2014) Oxytocin and vasopressin systems in genetic syndromes and neurodevelopmental disorders. Brain research 1580:199–218.

Froemke RC, Young LJ (2021) Oxytocin, Neural Plasticity, and Social Behavior. Annu Rev Neurosci 44:359–381.

Gimpl G, Fahrenholz F (2001) The oxytocin receptor system: structure, function, and regulation. Physiological Reviews 81:629–683.

Griffin GD, Ferri-Kolwicz SL, Reyes BAS, Van Bockstaele EJ, Flanagan-Cato LM (2010) Ovarian hormone-induced reorganization of oxytocin-labeled dendrites and synapses lateral to the hypothalamic ventromedial nucleus in female rats. J Comp Neurol 518:4531–4545.

Grinevich V, Knobloch-Bollmann HS, Eliava M, Busnelli M, Chini B (2016) Assembling the Puzzle: Pathways of Oxytocin Signaling in the Brain. Biological Psychiatry 79:155–164.

Grinevich V, Neumann ID (2020) Brain oxytocin: how puzzle stones from animal studies translate into psychiatry. Molecular Psychiatry:1–15.

Grinevich V, Stoop R (2018) Interplay between Oxytocin and Sensory Systems in the Orchestration of Socio-Emotional Behaviors. Neuron 99:887–904.

Guastella AJ, Hickie IB (2015) Oxytocin Treatment, Circuitry and Autism: A Critical Review of the Literature Placing Oxytocin into the Autism Context. Biological Psychiatry.

Hung LW, Neuner S, Polepalli JS, Beier KT, Wright M, Walsh JJ, Lewis EM, Luo L, Deisseroth K, Dölen G, Malenka RC (2017) Gating of social reward by oxytocin in the ventral tegmental area. Science (New York, NY) 357:1406–1411.

Jeong M, Kim Y, Kim J, Ferrante DD, Mitra PP, Osten P, Kim D (2016) Comparative three-dimensional connectome map of motor cortical projections in the mouse brain. Scientific reports 6:20072.

Jirikowski GF (2019) Diversity of central oxytocinergic projections. Cell Tissue Res 375:41–48.

Jurek B, Neumann ID (2018) The Oxytocin Receptor: From Intracellular Signaling to Behavior. Physiological Reviews 98:1805–1908.

Kemp AH, Guastella AJ (2010) Oxytocin: Prosocial Behavior, Social Salience, or Approach-Related Behavior? Biological Psychiatry 67:e33–e34.

Kim EJ, Jacobs MW, Ito-Cole T, Callaway EM (2016) Improved Monosynaptic Neural Circuit Tracing Using Engineered Rabies Virus Glycoproteins. Cell Rep 15:692–699.

Kim Y, Yang GR, Pradhan K, Venkataraju KU, Bota M, García Del Molino LC, Fitzgerald G, Ram K, He M, Levine JM, Mitra P, Huang ZJ, Wang X-J, Osten P (2017) Brain-wide Maps Reveal Stereotyped Cell-Type-Based Cortical Architecture and Subcortical Sexual Dimorphism. Cell 171:456-469.e22.

Klein S, Staring M, Murphy K, Viergever MA, Pluim JPW (2010) elastix: a toolbox for intensity-based medical image registration. IEEE transactions on medical imaging 29:196–205.

Knobloch HS, Charlet A, Hoffmann LC, Eliava M, Khrulev S, Cetin AH, Osten P, Schwarz MK, Seeburg PH, Stoop R, Grinevich V (2012) Evoked axonal oxytocin release in the central amygdala attenuates fear response. Neuron 73:553–566.

Knobloch HS, Grinevich V (2014) Evolution of oxytocin pathways in the brain of vertebrates. Front Behav Neurosci 8:31.

637 Kohara K, Pignatelli M, Rivest AJ, Jung HY, Kitamura T, Suh J, Frank D, Kajikawa K, Mise N,
638 Obata Y, Wickersham IR, Tonegawa S (2014) Cell type-specific genetic and optogenetic
639 tools reveal hippocampal CA2 circuits. Nature Neuroscience 17:269–279.

640 Lee H-J, Macbeth AH, Pagani JH, Young WS (2009) Oxytocin: the great facilitator of life.
641 Progress in neurobiology 88:127–151.

642 Li K, Nakajima M, Ibañez-Tallon I, Heintz N (2016) A Cortical Circuit for Sexually Dimorphic
643 Oxytocin-Dependent Anxiety Behaviors. Cell 167:60-72.e11.

644 Liao P-Y, Chiu Y-M, Yu J-H, Chen S-K (2020) Mapping Central Projection of Oxytocin
645 Neurons in Unmated Mice Using Cre and Alkaline Phosphatase Reporter. Front
646 Neuroanat 14 Available at:
647 https://www.frontiersin.org/articles/10.3389/fnana.2020.559402/full [Accessed January
648 17, 2021].

649 Madrigal M del P, Jurado S (2021) Specification of oxytocinergic and vasopressinergic circuits
650 in the developing mouse brain. Communications Biology 4:1–16.

651 Marlin BJ, Mitre M, D'amour JA, Chao M V, Froemke RC (2015) Oxytocin enables maternal
652 behaviour by balancing cortical inhibition. Nature 520:499–504.

653 Mens WB, Witter A, van Wimersma Greidanus TB (1983) Penetration of neurohypophyseal
654 hormones from plasma into cerebrospinal fluid (CSF): half-times of disappearance of
655 these neuropeptides from CSF. Brain research 262:143–149.

656 Mitre M, Marlin BJ, Schiavo JK, Morina E, Norden SE, Hackett TA, Aoki CJ, Chao MV,
657 Froemke RC (2016) A Distributed Network for Social Cognition Enriched for Oxytocin
658 Receptors. J Neurosci 36:2517–2535.

659 Nersesyan Y, Demirkhanyan L, Cabezas-Bratesco D, Oakes V, Kusuda R, Dawson T, Sun X,
660 Cao C, Cohen AM, Chelluboina B, Veeravalli KK, Zimmermann K, Domene C, Brauchi
661 S, Zakharian E (2017) Oxytocin Modulates Nociception as an Agonist of Pain-Sensing
662 TRPV1. Cell reports 21:1681–1691.

663 Newmaster KT, Nolan ZT, Chon U, Vanselow DJ, Weit AR, Tabbaa M, Hidema S, Nishimori K,
664 Hammock EAD, Kim Y (2020) Quantitative cellular-resolution map of the oxytocin
665 receptor in postnatally developing mouse brains. Nature communications 11:1885.

666 Osakada F, Mori T, Cetin AH, Marshel JH, Virgen B, Callaway EM (2011) New rabies virus
667 variants for monitoring and manipulating activity and gene expression in defined neural
668 circuits. Neuron 71:617–631.

669 Paxinos G, Franklin KBJ (2008) The Mouse Brain in Stereotaxic Coordinates. Academic Press.

670 Quintana DS, Guastella AJ (2020) An Allostatic Theory of Oxytocin. Trends in Cognitive
671 Sciences.

672 Raam T, McAvoy KM, Besnard A, Veenema AH, Sahay A (2017) Hippocampal oxytocin
673 receptors are necessary for discrimination of social stimuli. Nature communications
674 8:2001.

675 Ragan T, Kadiri LR, Venkataraju KU, Bahlmann K, Sutin J, Taranda J, Arganda-Carreras I, Kim
676 Y, Seung HS, Osten P (2012) Serial two-photon tomography for automated ex vivo
677 mouse brain imaging. Nature methods 9:255–258.

678 Rajamani KT, Wagner S, Grinevich V, Harony-Nicolas H (2018) Oxytocin as a Modulator of
679 Synaptic Plasticity: Implications for Neurodevelopmental Disorders. Frontiers in
680 Synaptic Neuroscience 10.

681 Renier N, Adams EL, Kirst C, Wu Z, Azevedo R, Kohl J, Autry AE, Kadiri L, Umadevi
682 Venkataraju K, Zhou Y, Wang VX, Tang CY, Olsen O, Dulac C, Osten P, Tessier-
683 Lavigne M (2016) Mapping of Brain Activity by Automated Volume Analysis of
684 Immediate Early Genes. Cell 165:1789–1802.

685 Ryan PJ, Ross SI, Campos CA, Derkach VA, Palmiter RD (2017) Oxytocin-receptor-expressing
686 neurons in the parabrachial nucleus regulate fluid intake. Nature Neuroscience 20:1722–
687 1733.

688 Sabihi S, Dong SM, Durosko NE, Leuner B (2014) Oxytocin in the medial prefrontal cortex
689 regulates maternal care, maternal aggression and anxiety during the postpartum period.
690 Frontiers in behavioral neuroscience 8:258.

691 Schiavo JK, Valtcheva S, Bair-Marshall CJ, Song SC, Martin KA, Froemke RC (2020) Innate
692 and plastic mechanisms for maternal behaviour in auditory cortex. Nature 587:426–431.

693 Shamay-Tsoory SG, Abu-Akel A (2015) The Social Salience Hypothesis of Oxytocin. Biol
694 Psychiatry.

695 Tang Y et al. (2020) Social touch promotes interfemale communication via activation of
696 parvocellular oxytocin neurons. Nature neuroscience.

697 Theodosis DT (1985) Oxytocin-immunoreactive terminals synapse on oxytocin neurones in the
698 supraoptic nucleus. Nature 313:682–684.

699 Tirko NN, Eyring KW, Carcea I, Mitre M, Chao M V, Froemke RC, Tsien RW (2018) Oxytocin
700 Transforms Firing Mode of CA2 Hippocampal Neurons. Neuron 100:593-608.e3.

701 Wang Q et al. (2020) The Allen Mouse Brain Common Coordinate Framework: A 3D Reference
702 Atlas. Cell 181:936-953.e20.

703 Wickersham IR, Lyon DC, Barnard RJO, Mori T, Finke S, Conzelmann K-K, Young JAT,
704 Callaway EM (2007) Monosynaptic restriction of transsynaptic tracing from single,
705 genetically targeted neurons. Neuron 53:639–647.

706 Yoshida M, Takayanagi Y, Inoue K, Kimura T, Young LJ, Onaka T, Nishimori K (2009)
707 Evidence that oxytocin exerts anxiolytic effects via oxytocin receptor expressed in
708 serotonergic neurons in mice. Journal of Neuroscience 29:2259–2271.

709 Zhang B, Qiu L, Xiao W, Ni H, Chen L, Wang F, Mai W, Wu J, Bao A, Hu H, Gong H, Duan S,
710 Li A, Gao Z (2020) Reconstruction of the Hypothalamo-Neurohypophysial System and
711 Functional Dissection of Magnocellular Oxytocin Neurons in the Brain. Neuron
712 Available at: http://www.sciencedirect.com/science/article/pii/S0896627320308564
713 [Accessed December 26, 2020].

714 Zheng JJ, Li SJ, Zhang X Di, Miao WY, Zhang D, Yao H, Yu X (2014) Oxytocin mediates early
715 experience-dependent cross-modal plasticity in the sensory cortices. Nature Neuroscience
716 17:391–399.

717

718 **Figure 1. Distribution of oxytocin neurons.**
719

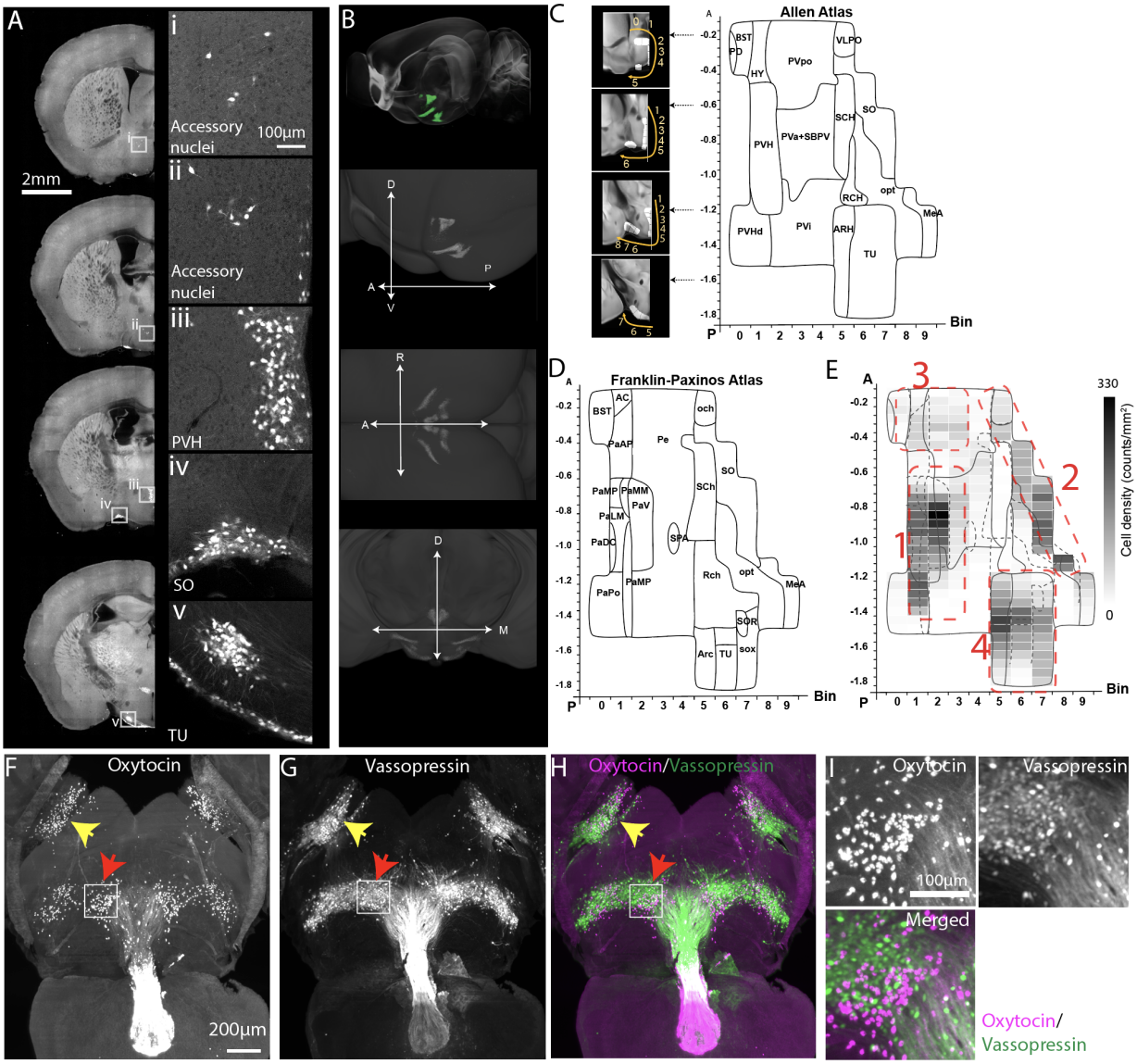

720

721 (A) Signals from OT-Cre;Ai14 mice across representative coronal planes of the mouse brain.
722 Figures on the right column are high magnification images from white boxed areas in the left
723 column. (B) (top) STPT images registered onto the Allen CCF reference brain. Green signals
724 represent averaged OT neurons from 8 animals. (bottom) 3D distribution of oxytocin neurons.
725 A/P: anterior/posterior, L/M: Lateral/medial, D/V: dorsal/ventral. See also Movie S1, Table 1.
726 (C-D) 2D hypothalamic flatmaps. Small inserts with coronal sections illustrate how bins (while
727 areas with numbers) were generated at different coronal planes. Anatomical labels in the flatmap
728 are delineated based on Allen mouse brain atlas (C) and Franklin-Paxinos atlas (D). The X-axis
729 is for bin numbers and Y-axis is for the bregma A/P axis. The full name of abbreviations can be
730 found in Table 1. (E) Heatmap of oxytocin neuronal density in four clusters with the overlay of
731 Allen and Franklin-Paxinos labels in solid and dotted lines, respectively. Red dotted lines for
732 four OT expressing domains. 1: PVH, 2: SO, 3: AN, and 4: TU. (F-I) Light sheet fluorescence
733 microscopy imaging of whole brain immunostaining with OT and vasopressin antibodies. 500

734 μm thick z maximum projection of OT (F), vasopressin (G), and both (H). Yellow and red
735 arrows for the SO and the TU, respectively. (I) high magnification images from the white boxed
736 TU area in (F-G), Note the lack of colocalization between the OT and vasopressin.
737
738

Figure 2. Anterograde projection map of oxytocin neurons.

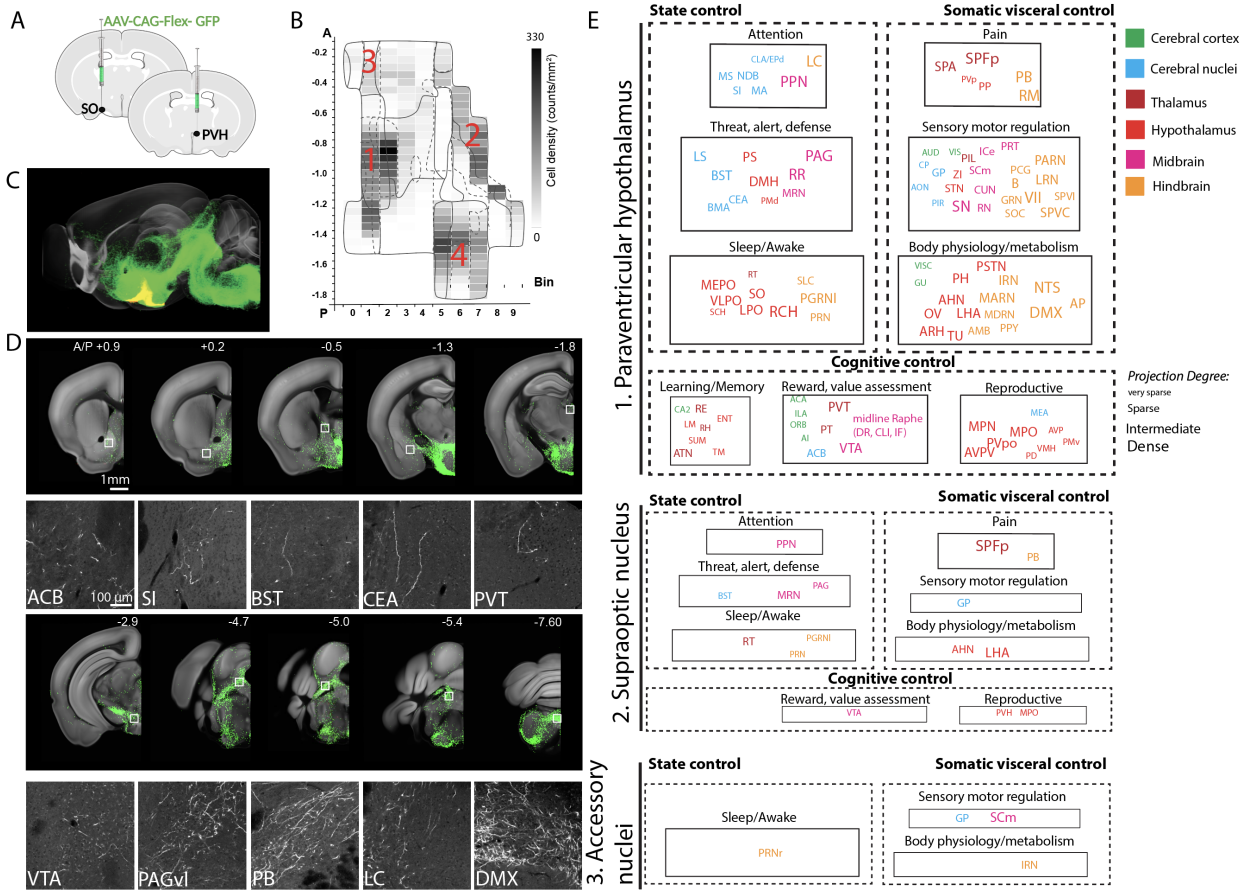

(A) Conditional AAV-GFP was injected in OT neuron containing hypothalamic areas. (B) Four major areas of viral injections, 1: the PVH, 2: the SO, 3: the AN, 4: the TU area. (C) Projection outputs from the PVH (green) and SO (yellow) oxytocin neurons registered in the Allen CCF. See also Movie S2. (D) Examples of long-range projections (green) from OT neurons in the PVH. The bottom panel is high mag images from white boxed areas in the top panel. (E) Nine functional circuits that receive long-range projection from OT neurons in the three different injection area 1 - 3. Color and size of each region of interest represent anatomical ontology and the abundance (degree) of the projection. The full name of abbreviations can be found in Table 2.

Figure 3. Comparison between the oxytocin output and oxytocin receptor expression.

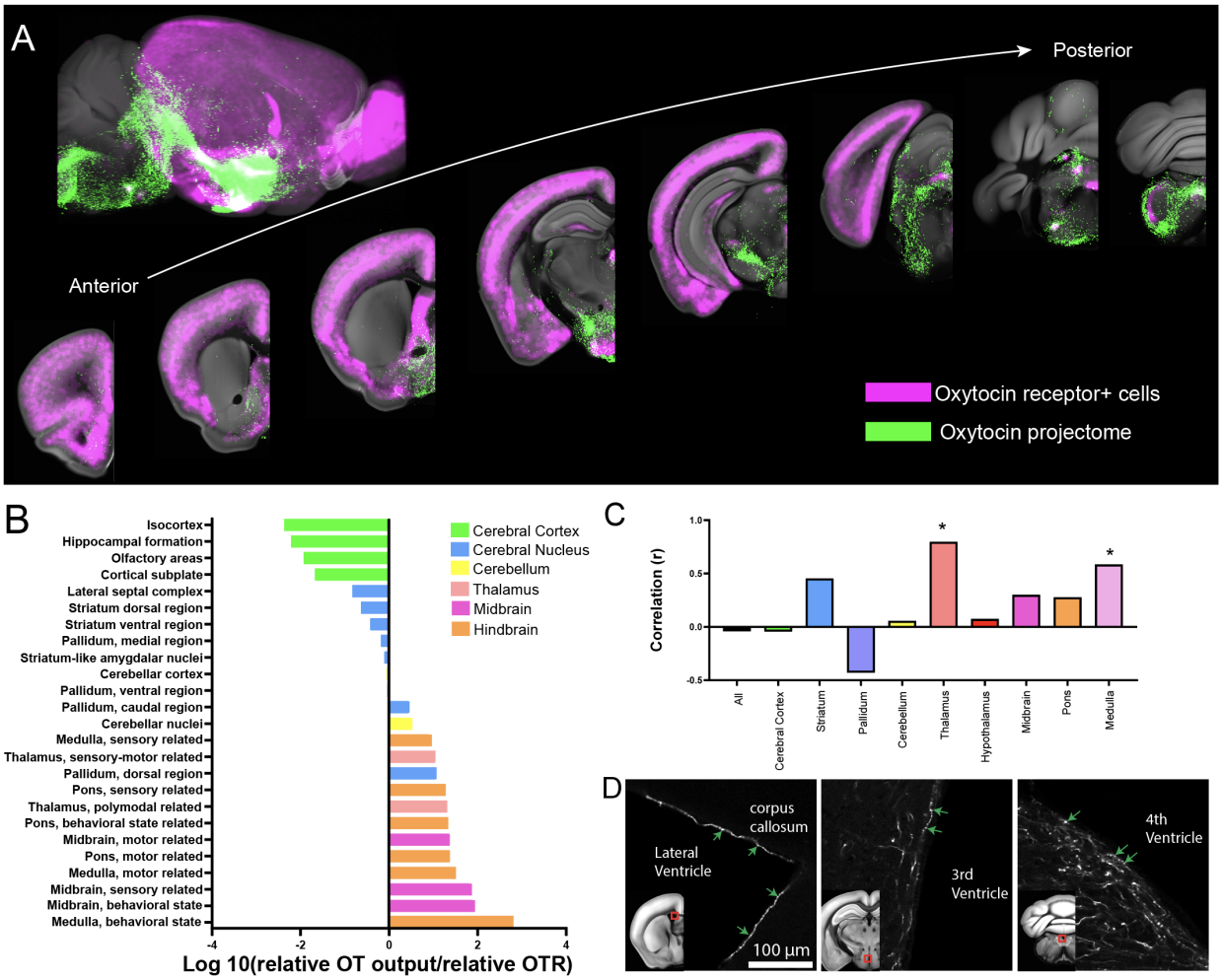

(A) Composite images of representative OT neuronal projection outputs (red: combined from both the PVH and the SO) and OTR expression (green) across the mouse brain. See also Movie S3. (B) Quantitative comparison of relative OT projection pattern and OTR expression. Note that the cerebral cortex has very small OT/OTR ratio while the hindbrain and the midbrain shows higher ratio. (C) Correlation between OT projection and oxytocin receptor density (Spearman nonparametric correlation, *: $p<0.05$). Note no significant correlation across the whole brain areas despite the significant correlation in the thalamus and the medulla. (D) Examples of OT long range projection touching the surface of all major ventricles.

Figure 4. Monosynaptic input map of oxytocin neurons in the PVH and the SO.

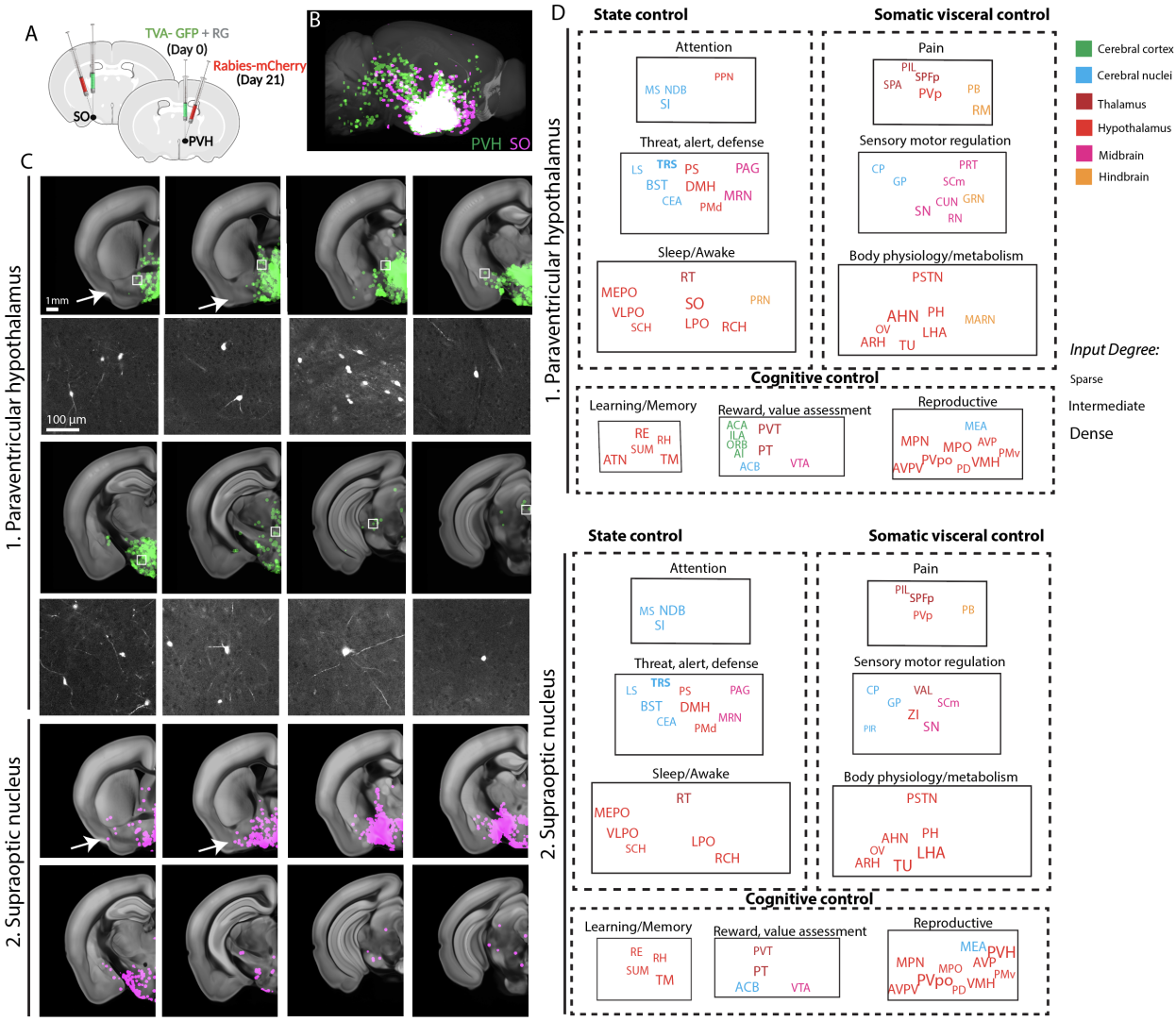

(A) Conditional mono-synaptic tracing rabies virus was injected in the PVH or the SO of the OT-Cre mice. (B) Brain-wide inputs into the PVH (green, n = 6 animals) and SO (red, n = 4 animals) OT neurons. The maximum signals of all samples from each anatomical region were overlaid on the reference brain. See also Movie S4. (C) Representative mono-synaptic inputs in different coronal planes (top panel) and high mag images from white boxed areas (bottom panel). Arrows highlight input from lateral brain areas for the SO compared to the PVH. (D) Nine functional circuits that provide mono-synaptic input to OT neurons in the two anatomical areas. Note overall similar input patterns for both areas. The full name of abbreviations can be found in Table 2.

778 **Figure 5. OT input-output wiring diagram**
779

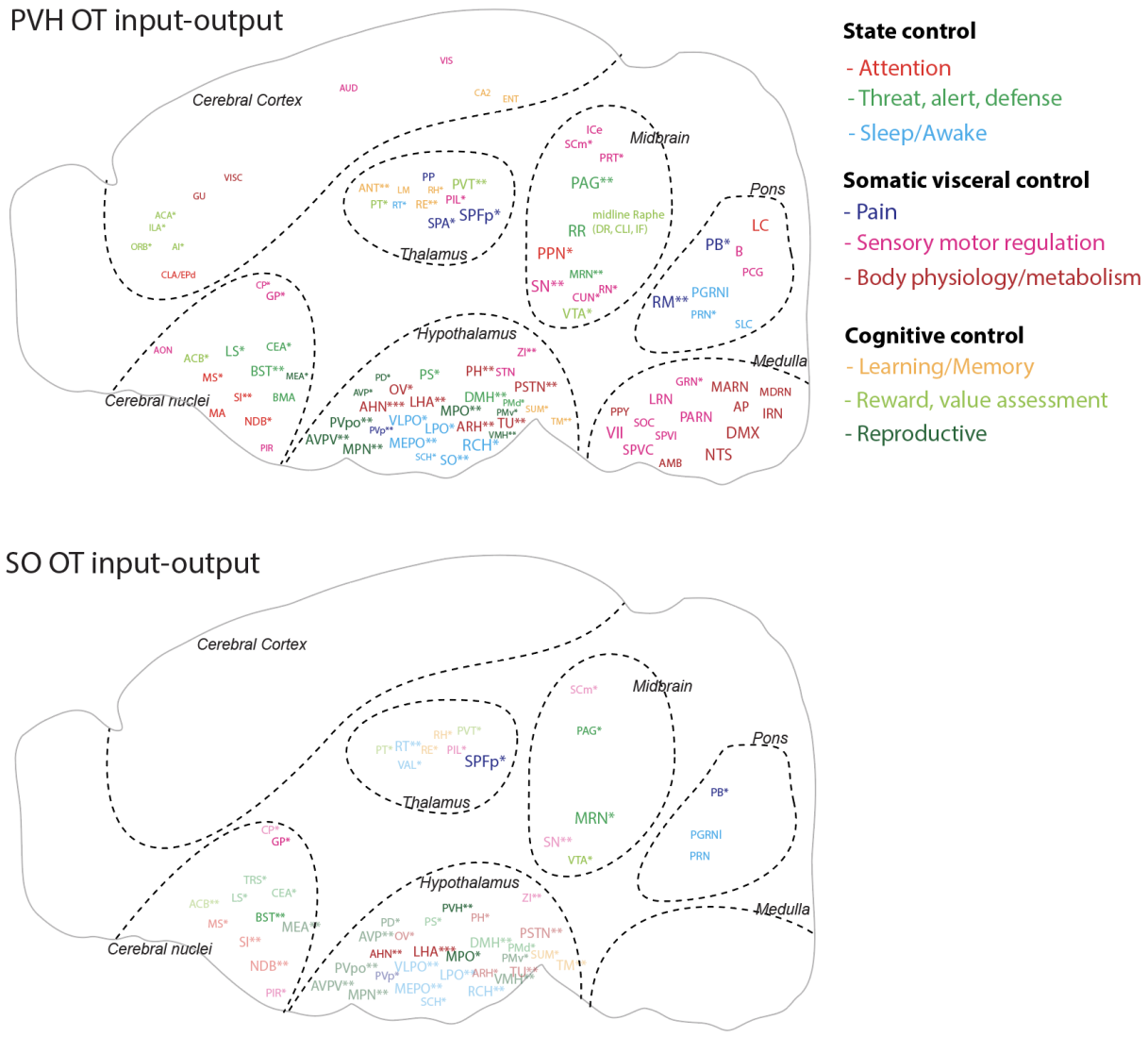

780
781 Schematic summary of mono-synaptic input and axonal output connectivity of OT neurons.
782 Color of each ROI is related to nine functional circuits. ROI size is correlated with OT output
783 degree as done in Figure 2. Areas providing the monosynaptic input are highlighted with asterisk
784 (*). Number of * indicated input strength: * < 10 cells, 10 ≤ ** < 100, 100 ≤ ***. Monosynaptic
785 input areas without receiving OT output in the SO-OT map were indicated with semi-transparent
786 fonts. All abbreviations for brain regions can be found in Table 2.
787
788
789

Table 1. Oxytocin neuron counting

Cluster	Full Names	Abbreviations	Transgenic	3D immuno labeling
1	Paraventricular hypothalamic nucleus	PVH	511.5 ± 147.1	818 ± 169
	Periventricular hypothalamic nucleus, anterior part	PVa	47.6 ± 22.7	119 ± 23
	Periventricular hypothalamic nucleus, intermediate part	PVi	9.6 ± 11.4	14 ± 5
	Subparaventricular zone	SBPV	17.9 ± 20.8	113 ± 49
	Paraventricular hypothalamic nucleus, descending division	PVHd	153.8 ± 49.7	27 ± 16
2	Supraoptic nucleus	SO	202.3 ± 65.5	654 ± 89
	Medial amygdalar nucleus	MEA	108.7 ± 49.6	10 ± 4
	Ventrolateral preoptic nucleus	VLPO	21.9 ± 23.3	50 ± 20
3	Bed nuclei of the stria terminalis	BST	27.8 ± 11	68 ± 34
	Periventricular hypothalamic nucleus, preoptic part	PVpo	51.1 ± 18.3	194 ± 40
	Substantia innominata	SI	6 ± 3.1	2 ± 2
	Medial preoptic nucleus	MPN	18 ± 5.8	71 ± 14
	Lateral hypothalamic area	LHA	45.9 ± 14.4	32 ± 12
	Lateral preoptic area	LPO	2.1 ± 2	4 ± 2
4	Tuberal nucleus	TU	472.9 ± 65.2	393 ± 121
	Arcuate hypothalamic nucleus	ARH	147.5 ± 86.5	272 ± 83

Transgenic animal counting is from serial two-photon tomography imaging of OT-Cre;Ai14 mice (n=8) and 3D immunolabeling counting is from light sheet fluorescence microscopy imaging of C57 after tissue clearing and 3D oxytocin antibody staining (n=7). Counting data are mean ± standard deviation.

798 **Table 2. Nine functional circuits that are connected with oxytocin neurons.**
799

Functional Circuits	Full Name	Abbreviation
Attention	Medial septal nucleus	MS
	Diagonal band nucleus	NDB
	Substantia innominata	SI
	Medial septal nucleus	MS
	Claustrum/dorsal endopiriform nucleus	CLA/EPd
	Locus ceruleus	LC
	Pedunculopontine nucleus	PPN
Threat, alert, defense	Lateral septal nucleus	LS
	Bed nuclei of the stria terminalis	BST
	Central amygdalar nucleus	CEA
	Basal medialy amygdala	BMA
	Parastrial nucleus	PS
	Dorsomedial nucleus of the hypothalamus	DMH
	Dorsal premammillary nucleus	PMd
	Periaqueductal gray, ventral lateral	PAG
	Midbrain reticular nucleus, retrorubral area	RR
	Midbrain reticular nucleus	MRN
Sleep/Awake	Median preoptic nucleus	MEPO
	Ventrolateral preoptic nucleus	VLPO
	Suprachiasmatic nucleus	SCH
	Reticular Thalamus	RT
	Supraoptic nucleus	SO
	Lateral preoptic area	LPO
	Subceruleus nucleus	SLC
	Retrochiasmatic area	RCH
	Paragigantocellular reticular nucleus, lateral part	PGRNl
	Pontine reticular nucleus	PRN
Pain	Subparafascicular area	SPA
	Subparafascicular nucleus, posterior	SPFp
	Periventricular hypothalamic nucleus, posterior part	PVp
	Peripeduncular nucleus	PP
	Parabrachial nucleus	PB
	Nucleus raphÈ magnus	RM
Sensory motor regulation	Auditory cortex	AUD
	Visual cortex	VIS
	Caudate Putamen	CP

	Globus pallidus	GP
	Anterior olfactory nucleus	AON
	Piriform cortex	PIR
	Posterior Intralaminar Thalamic nucleus	PIL
	Zona Incerta	ZI
	Subthalamic nucleus	STN
	Substantia niagra	SN
	Inferior colliculus, external nucleus	ICe
	Superior colliulus, motor	SCm
	Cuneiform nucleus	CUN
	Red nucleus	RN
	Pretectal region	PRT
	Pontine central gray	PCG
	Barrington's nucleus	B
	gigantocellular reticular nucleus	GRN
	Superior olivary complex	SOC
	Parvicellular reticular nucleus	PARN
	Lateral reticular nucleus	LRN
	Facial motor nucleus	VII
	Spinal nucleus of the trigeminal, caudal part	SPVC
	Spinal nucleus of the trigeminal, interpolar part	SPVI
Body physiology/metabolism	Visceral cortex	VISC
	Gustatory cortex	GU
	Parasubthalamic nucleus	PSTN
	Posterior hypothalamic nucleus	PH
	Anterior hypothalamic nucleus	AHN
	Vascular organ of the lamina terminalis	OV
	arcuate hypothalamic nucleus	ARH
	Lateral hypothalamic area	LHA
	Tuberal nucleus	TU
	Intermediate reticular nucleus	IRN
	Magnocellular reticular nucleus	MARN
	Medullary reticular nucleus	MDRN
	Nucleus ambiguus	AMB
	Parapyramidal nucleus	PPY
	Nucleus of the solitary tract	NTS
	Dorsal motor nucleus of the vagus nerve	DMX
	Area postrema	AP
Learning and Memory	Field CA2	CA2

	Nucleus of reunions	RE
	Lateral mammillary nucleus	LM
	Rhomboid nucleus	RH
	Supramammillary nucleus	SUM
	Anterior group of dorsal thalamus	ATN
	Entorhinal area	ENT
	Tuberomammillary nucleus	TM
Reward, value assessment	Anterior cingulate area	ACA
	Infralimbic cortex	ILA
	Orbital cortex	ORB
	Agranular insular area	AI
	Nucleus accumbens	ACB
	Paraventricular nucleus of the thalamus	PVT
	Parataenial nucleus	PT
	Dorsal Raphe	DR
	Central linear nucleus raphe	CLI
	Interfascicular nucleus raphe	IF
	Ventral tegmental area	VTA
Reproductive	Medial preoptic nucleus	MPN
	Periventricular hypothalamic nucleus, preoptic part	PVpo
	Anteroventral periventricular nucleus	AVPV
	Medial preoptic area	MPO
	Anteroventral preoptic nucleus	AVP
	Ventral premammillary nucleus	PMv
	Ventromedial hypothalamic nucleus	VMH
	Posterodorsal preoptic nucleus	PD
	Medial amygdala	MEA

800
801